



Formation of the Lyman Continuum during Solar Flares

Shaun A. McLaughlin¹, Ryan O. Milligan^{1,2}, Graham S. Kerr^{2,3}, Aaron J. Monson¹, Paulo J. A. Simões^{4,5}, and Mihalis Mathioudakis¹

¹Queen's University Belfast, University Road, Belfast BT7 1NN, UK

²Department of Physics, Catholic University of America, 620 Michigan Avenue Northeast, Washington, DC 20064, USA

³Solar Physics Laboratory (Code 671), Heliophysics Science Division, NASA Goddard Space Flight Center, Greenbelt, MD 20771, USA

⁴Center for Radio Astronomy and Astrophysics Mackenzie, School of Engineering, Mackenzie Presbyterian University, São Paulo, Brazil

⁵SUPA, School of Physics & Astronomy, University of Glasgow, Glasgow G12 8QQ, UK

Received 2022 September 9; revised 2022 December 16; accepted 2022 December 31; published 2023 February 23

Abstract

The Lyman continuum (LyC; $<911.12 \text{ \AA}$) forms at the top of the chromosphere in the quiet Sun, making LyC a powerful tool for probing the chromospheric plasma during solar flares. To understand the effects of nonthermal energy deposition in the chromosphere during flares, we analyzed LyC profiles from a grid of field-aligned radiative-hydrodynamic models generated using the RADYN code as part of the F-CHROMA project. The spectral response of LyC, the temporal evolution of the departure coefficient of hydrogen, b_1 , and the color temperature, T_c , in response to a range of nonthermal electron distribution functions, were investigated. The LyC intensity was seen to increase by 4–5.5 orders of magnitude during solar flares, responding most strongly to the nonthermal electron flux of the beam. Generally, b_1 decreased from 10^2 – 10^3 to closer to unity during solar flares, indicating a stronger coupling to local conditions, while T_c increased from 8–9 to 10–16 kK. T_c was found to be approximately equal to the electron temperature of the plasma when b_1 was at a minimum. Both optically thick and optically thin components of LyC were found to be in agreement with the interpretation of recent observations. The optically thick layer forms deeper in the chromosphere during a flare compared to quiescent periods, whereas the optically thin layers form at higher altitudes due to chromospheric evaporation, in low-temperature, high-density regions propagating upward. We put these results in the context of current and future missions.

Unified Astronomy Thesaurus concepts: Solar flares (1496); Solar chromosphere (1479)

1. Introduction

Solar flares are the most energetic events occurring in the solar system, releasing up to 10^{32} erg of energy over the course of tens of minutes (Fletcher et al. 2011). This energy is typically thought to be released via magnetic reconnection in the solar corona. Following release, this energy manifests itself in several ways, including in the acceleration of large quantities of charged particles that propagate along magnetic field lines, deeper into the Sun's atmosphere. These charged particles undergo Coulomb collisions with the ambient plasma depositing energy in the solar chromosphere, where intense heating, ionization, and mass flows result. The subsequent increase in radiation allows us to shed light on the physical mechanisms that release and transport energy. Modeling by Allred et al. (2005) suggests that solar flare emission is energetically dominated by the Balmer continuum. However, Balmer continuum observations have been severely lacking. Lyman continuum (LyC) flare observations have been more readily available in recent years from the Extreme Ultraviolet Experiment (EVE; Woods et al. 2012) on board the Solar Dynamic Observatory (SDO; Pesnell et al. 2012), with the potential of upcoming flare observations from the Spectral Imaging of the Coronal Environment (SPICE; Spice Consortium et al. 2020) instrument on board the Solar Orbiter (Müller et al. 2020), and the EUV High-Throughput

Spectroscopic Telescope (EUVST; Shimizu et al. 2019) on board Solar-C (Watanabe 2014).

LyC $< 911.12 \text{ \AA}$ results from the free-bound transition of a free electron to the ground state of ambient hydrogen nuclei. In the quiet Sun, LyC forms at the top of the chromosphere/base of the transition region where the temperature rises from the cooler, denser chromosphere ($T \leq 10^4 \text{ K}$) to the corona, ($T \geq 10^6 \text{ K}$; Vernazza et al. 1973, 1976, 1981; Avrett & Loeser 2008; Machado et al. 2018). Therefore, the LyC is sensitive to energy perturbations in the chromosphere induced during solar flares, and since thermalization occurs very rapidly at the higher densities located there, its spectrum may reflect the local plasma temperature (Noyes & Kalkofen 1970). The LyC is a potentially powerful diagnostic tool of the chromospheric response to flare energy injection, but this potential is presently largely untapped.

One of the earliest investigations into LyC formation during solar flares was performed by Machado & Noyes (1978), who observed nine flares using the extreme ultraviolet (EUV) spectrograph on the Apollo Telescope Mount on board Skylab (Ise & Cagle 1974). They found that the nonlocal thermodynamic equilibrium (NLTE) departure coefficient of the first level of hydrogen (b_1) tended toward unity during flares, more so than in active regions or the quiet Sun. The departure coefficient is given by n_1/n_1^* , where n_1^* is the ground state LTE population and n_1 is the NLTE ground state populations, meaning the LyC formation region was driven closer to LTE conditions during the solar flares (Menzel & Cillie 1937). They also found that the color temperature (T_c) derived from the head of the continuum was around $T_c \sim 7.9$ – 9 kK , comparable to that of the surrounding quiet Sun, but hotter than active



Original content from this work may be used under the terms of the [Creative Commons Attribution 4.0 licence](https://creativecommons.org/licenses/by/4.0/). Any further distribution of this work must maintain attribution to the author(s) and the title of the work, journal citation and DOI.

regions. They concluded that in flares LyC is optically thick and forms close to LTE in a region of higher density deeper in the chromosphere, whereas in active regions or the quiet Sun $b_1 \approx 10^2$ (Noyes & Kalkofen 1970). However, they also showed that T_c measured at shorter wavelengths (700–790 Å) revealed higher temperatures (10–15 kK, although with large uncertainties), suggesting the presence of an optically thin LyC layer that formed higher in the atmosphere. One limitation of this study was that several of the observations were carried out in spectral scanning mode; spectra were obtained in a 5 arcsec² area over 300–1335 Å, over 3.8 minutes, meaning that different parts of the spectrum may have been sampled at different times and may not reflect true changes due to the flare.

More recently, Machado et al. (2018) performed a study using Sun-as-a-star observations from EVE on board SDO, which allowed the temporal evolution of LyC emission during six major solar flares to be investigated. After converting the EVE data from spectral irradiance to specific intensity, by assuming flaring areas, they reported that the LyC intensities at the head of the continuum were enhanced by 3–4 orders of magnitude relative to pre-flare values. Their results supported the earlier conclusions of Machado & Noyes (1978). However, Machado et al. (2018) found a larger color temperature, noting that T_c determined between 870 and 912 Å increased from $T_c = 8\text{--}9$ kK to $\approx 9\text{--}12$ kK, perhaps due to the study of more energetic events.

Milligan et al. (2012) reported an enhancement in LyC emission during an X-class flare that occurred on 2011 February 15 also using data from SDO/EVE. A follow-up study showed that the total energy radiated by LyC was a few percent of the total nonthermal electron energy, amounting to 1.8×10^{29} erg over the course of the flare, comparable to the radiated soft X-ray energy (Milligan et al. 2014). LyC irradiance increased by approximately a factor of 10 during the impulsive phase.

Lemaire et al. (2004) presented observations of an X5.3 solar flare from the head of the LyC obtained from scattered light detected by the Solar Ultraviolet Measurements of Emitted Radiation spectrometer (Wilhelm et al. 1995) on board the Solar and Heliospheric Observatory (Domingo et al. 1995) mission. They determined the local increase in LyC radiance to be a factor of several thousand, in agreement with Machado & Noyes (1978). Using the ratio of the spectral radiance at 910 and 890 Å they estimated $T_c = 12.15$ kK.

There have been several attempts at modeling LyC during solar flares. Ding & Schleicher (1997) calculated LyC intensities in response to a precipitating beam of nonthermal particles using a non-LTE, radiative transfer code. They found that LyC is very sensitive to the incoming flux of electrons, and they predicted that the temperature at the formation height of LyC will increase in conjunction with a downward shift of the transition region. In particular, they noted that nonthermal collisions were responsible for driving down b_1 . In their experiments, Ding & Schleicher (1997) manually modified semiempirical model atmospheres to investigate the impact of the chromospheric temperature gradients, and transition region depth on the LyC formation, in a manner that was not self-consistent (i.e., they did not simulate the time-dependent chromospheric radiation-hydrodynamic response to energy injection by a beam of nonthermal electrons). For the purposes of including nonthermal collisional ionization of hydrogen, they assumed nonthermal electron fluxes of $F = [10^{10}, 10^{11},$

$10^{12}] \text{ erg cm}^{-2} \text{ s}^{-1}$, with spectral indices $\delta = [3, 4, 5]$, and a fixed low-energy cutoff of $E_c = 20$ keV. They found that LyC intensities increased by 1–3 orders of magnitude compared to the quiet-Sun values, and that the LyC intensities were highly sensitive to the flux of the nonthermal electron beam. The LyC intensities were less sensitive to the spectral index of the nonthermal electron distribution.

More recent modeling of LyC emission was performed by Druett & Zharkova (2019) using the radiation transport and hydrodynamic code, HYDRO2GEN. They investigated the spectral response of LyC to various electron beam fluxes during the impulsive and gradual phases of solar flares. They found that the LyC intensities increased by 2 orders of magnitude from their F10 model to their F12 model, highlighting the sensitivity of the LyC intensities to the flux of the nonthermal electron beam. From continuum contribution functions, they determined that LyC forms under optically thick conditions at the top of the chromosphere. During the impulsive phase, they noted a flattening of the LyC spectra but found that the gradient steepened further from the head of the continuum, in agreement with Machado & Noyes (1978) and Machado et al. (2018). During the gradual phase, however, they observed a flattening of the LyC spectra at shorter wavelengths compared to the impulsive phase spectra. They stated that the flattening below 700 Å is due to emission from high-altitude regions that cool sufficiently to allow recombinations to occur, resulting in an enhanced intensity longward of ~ 700 Å.

In this paper, we build upon these prior modeling efforts, by investigating the plasma properties (namely, T_c and b_1) in the region of LyC formation, and the diagnostic potential of the LyC in flares. We present a detailed analysis of LyC emission from a large parameter space of solar flare models using the Flare CHROMospheres: Observations, Models and Archives (F-CHROMA⁶) grid of models generated by the 1D field-aligned radiative-hydrodynamic code RADYN. The analysis of the models is provided in the results sections of the paper.

2. Numerical Simulations

RADYN is a 1D field-aligned radiative-hydrodynamic code that solves the coupled time-dependent equations of hydrodynamics, NLTE radiative transfer, nonequilibrium atomic level populations, and charge conservation (Carlsson & Stein 1992, 1995, 1997; Allred et al. 2005, 2015). The code's adaptive grid (Dorfi & Drury 1987) allows RADYN to resolve steep gradients or shocks that easily form in flares. RADYN solves the NLTE radiation transfer for a six-level hydrogen atom, a nine-level helium atom, and a six-level Ca II ion.

Important for modeling the LyC, RADYN models the nonequilibrium populations, and for hydrogen and helium includes nonthermal collisional rates between the injected nonthermal electron distribution and ambient plasma. For helium, we use the expressions from Arnaud & Rothenflug (1985) to model nonthermal collisional ionization of He I \rightarrow He II, and from He II \rightarrow He III. For hydrogen, we include nonthermal collisional ionization from the ground state, and excitation from the ground state to $n = [2, 3, 4]$, following the approach of Fang et al. (1993). In this approach, we are able to include the important effects of secondary collisions. As discussed in several prior studies (e.g., Ricchiazzi & Canfield 1983; Fang et al. 1993;

⁶ <https://star.pst.qub.ac.uk/wiki/public/solarmodels/start.html>

Karlicky et al. 2004; Kasparova et al. 2009), nonthermal collisional ionization from the excited states are of lesser importance, in part because the population of the excited states is orders of magnitude smaller than the ground state. Thus, the ionization stratification is unlikely to be drastically altered by the omission of nonthermal collisions from the ground state. Note, however, that some models have included nonthermal effects from the excited states (see, e.g., Zharkova & Kobylinsky 1993; Druett & Zharkova 2018) though it is unclear just how much of a role those collisions played compared to those from the ground state. Figure 3 of Zharkova & Kobylinsky (1993) does show that nonthermal collisions from $n = 2$ became important relative to the thermal collisional rates, but only deep in the atmosphere. For the reasons that we discussed above, and since we are focused on the LyC that forms in the upper chromosphere/lower transition region, we believe that we are justified in using only ground state nonthermal collisional rates including secondary effects.

RADYN is a well-established resource that has been extensively used to model the response of the solar atmosphere to flare energy injection (e.g., Abbett & Hawley 1999; Allred et al. 2005; Kennedy et al. 2015; Kowalski et al. 2015; Allred et al. 2015; Kerr et al. 2016; Rubio da Costa et al. 2016; Simoes et al. 2017; Kowalski et al. 2017; Kowalski & Allred 2018; Brown et al. 2018; Kerr et al. 2019; Graham et al. 2020; Kerr et al. 2020, 2021; Kowalski et al. 2022). When simulating flares driven by electron beams (the *standard model*) the nonthermal electron distribution is modeled as a power law characterized by the spectral index, δ , the low-energy cutoff, E_c , and energy flux density, F . The transport and thermalization of these nonthermal electrons are modeled by solving the Fokker–Planck equations, including various diffusion terms (Allred et al. 2015). Note that we solve the Coulomb operator using general forms of the Rosenbluth potentials and so no assumption is made as to the target temperature; that is, there is no need to make a cold or warm target approximation (see also Allred et al. 2020). Beam parameters can be obtained through backward modeling of hard X-ray observations taken with space-borne satellites such as the Ramaty High Energy Solar Spectroscopic Imager (Lin et al. 2002) or the Fermi Gamma-Ray Space Telescope (Meegan et al. 2009), usually under the assumption of thick target collisions (Brown 1971; Holman et al. 2003; Krucker et al. 2007; Kontar et al. 2008; Krucker et al. 2008). In our study, we do not model a specific flare, but instead survey a large parameter space of δ , E_c , and F values, with the values of those parameters guided by typical observed ranges (e.g., Holman et al. 2011; Kontar et al. 2011).

The F-CHROMA grid of RADYN flare models, hosted by Queen’s University Belfast, consists of 72 RADYN simulations (M. Carlsson 2022, in preparation) This grid includes $\delta = [3, 4, 5, 6, 7, 8]$, and $E_c = [10, 15, 20, 25]$ keV, and models various magnitudes of injected nonthermal electron flux as a 20 s triangular profile in time, peaking at $t = 10$ s. The time-integrated energy flux ranges are $F_{\text{tot}} = [3 \times 10^{10}, 1 \times 10^{11}, 3 \times 10^{11}, 1 \times 10^{12}]$ erg cm⁻². It is typical in the flare community to refer to the energy flux density, and so for the remainder of this paper we quote the peak injected flux (at $t = 10$ s in each simulation), which are $F = [3 \times 10^9, 1 \times 10^{10}, 3 \times 10^{10}, 1 \times 10^{11}]$ erg cm⁻² s⁻¹. For brevity, we refer to these simulations as, e.g., 1F11, equating to 1×10^{11} erg cm⁻² s⁻¹.

Table 1
Nonthermal Electron Beam Parameters Used for Generating the RADYN Models Analyzed in this Work

F (erg cm ⁻² s ⁻¹)	δ	E_c (keV)
3×10^9	3, 4, 5, 6, 7	15, 20, 25
1×10^{10}	3, 4, 5, 6, 7	15, 20, 25
3×10^{10}	3, 4, 5, 6, 7	15, 20, 25
1×10^{11}	3, 4, 5	20, 25

In this study, we have selected 25 of the 72 models (Table 1). Not every combination of δ and E_c was modeled for inclusion in this grid for the highest energy flares. The models omitted from our subset are the 1F11, $E_c = 20$ keV, $\delta = [6, 7]$, models and the 1F11, $\delta = 5$, $E_c = 15$ keV model.

3. LyC Response to Flare Energy Injection

3.1. Synthetic LyC Spectra

Figure 1 shows continuum spectra at the time of the peak LyC emission in each simulation, between 9.7 and 13.6 s. The He I edge at 503.98 Å is also visible. The top row shows spectra generated for a fixed low-energy cutoff of 20 keV, while increasing the beam flux from 3F9 to 1F11 (left to right), and varying the spectral indices from $\delta = 3$ –7 (colored lines). The pre-flare spectra are shown in black. There were some snapshots (<1 s) in a few simulations in which the EUV continua tails had negative intensities, likely due to numerical noise. The simulations where the LyC was affected are the 3F10, $\delta = 5$, $E_c = 20$ keV model and the 1F10, $\delta = 5$, $E_c = 20$ keV model. Therefore, the spectra shown for these models have been shifted by 1 s. The spectra for the models where only the Ca II continuum was affected were not shifted. As the electron beam intensifies, so too does the response of LyC, peaking roughly coterminally with the peak of the heating rate. The 1F11, $\delta = 4$, 20 keV model is an exception, peaking at a time of 13.6 s as will be discussed in Section 3.2. For the 3F9 models, the head of the continuum is around 4 orders of magnitude greater than the pre-flare value. This increases to around 5.5 orders of magnitude for the 1F11 models. The magnitude of the LyC enhancement during solar flares is strongly dependent on the flux of nonthermal electrons. The dependence on the spectral index of the beam is weaker; softer beams result in slightly higher intensities. This is because softer beams (larger δ) deposit their energy over a narrower region in the upper chromosphere since they thermalize more easily, resulting in more localized heating and electron density enhancements.

The bottom row of Figure 1 shows synthetic LyC spectra for a fixed spectral index of $\delta = 5$ and $E_c = [15, 20, 25]$ keV (colored lines). The LyC spectra are weakly dependent on the low-energy cutoff, similar to the behavior seen with varying the spectral index; beams with larger E_c values are composed of a greater proportion of high-energy electrons that penetrate deeper into the atmosphere, resulting in the beam heating region shifting downward, affecting the LyC response. The increase in intensity from varying the spectral index and low-energy cutoff is much weaker compared with that caused by the increasing flux of the nonthermal electrons.

Like Ding & Schleicher (1997), we found a strong dependence of the LyC spectral intensity upon the flux of the nonthermal electron beam, as can be seen in Figure 1.

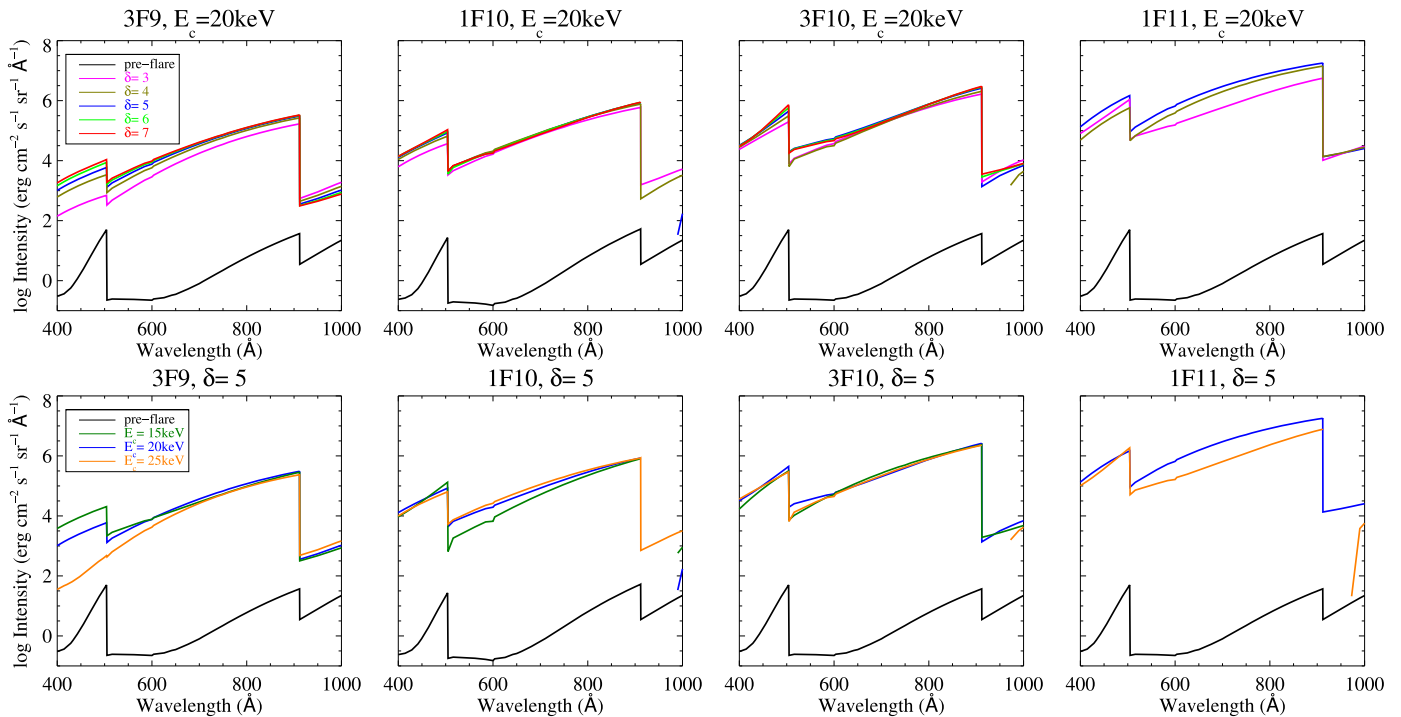


Figure 1. Synthetic RADYN continua spectra from 400–1000 Å showing the head of the He I continuum (<503.98 Å), LyC (<911.12 Å), and the tail of the Ca II continuum (<1044.00 Å). The top row shows spectra for a fixed $E_c = 20$ keV, with peak beam fluxes of 3F9, 1F10, 3F10, and 1F11, all shown at the peak in the LyC spectrum (between 9.7 and 13.6 s for all models). The black curve denotes the pre-flare spectra, while the colored curves show the spectra for spectral indices of $\delta = 3$ –7. The bottom row shows the spectra but for a fixed $\delta = 5$, varying $E_c = 15$, 20, and 25 keV. Note the 3F10, $\delta = 5$, $E_c = 20$ keV and the 1F10, $\delta = 5$, $E_c = 20$ keV models have transient negative intensities in the tail of the LyC continuum at the time of the peak LyC emission. This is due to numerical noise in the simulation at these times, which only lasts a very short amount of time. Therefore, the spectra shown for these models have been shifted by 1 s.

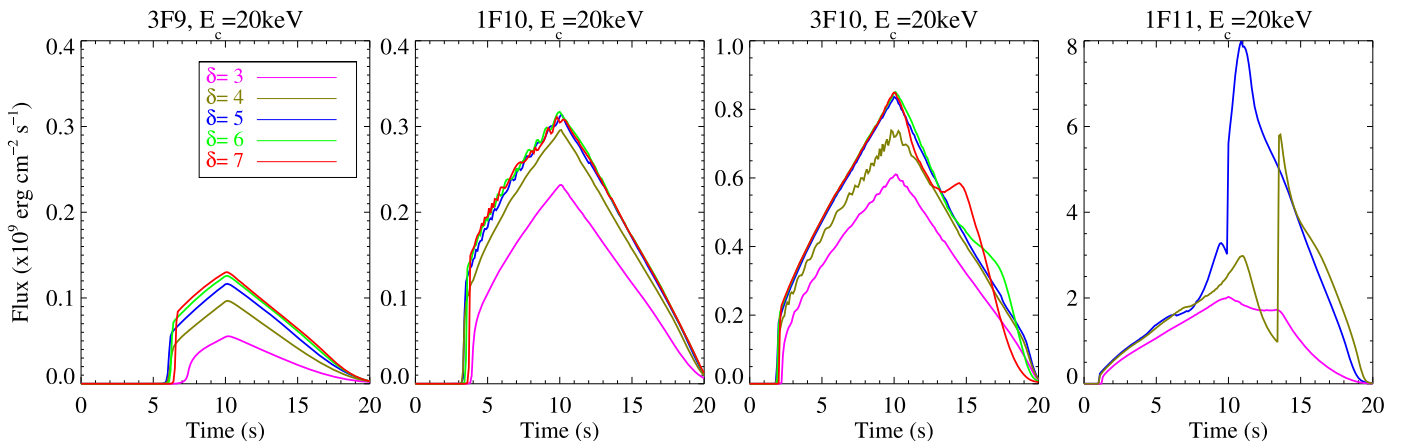


Figure 2. Flare excess light curves of spectrally integrated LyC emission from RADYN (505.0–911.7 Å) for the 3F9, 1F10, 3F10, and 1F11 models with $\delta = 3$ –7 and $E_c = 20$ keV.

However, RADYN predicts larger impulsive phase LyC intensities than the modeling of Ding & Schleicher (1997). Ding & Schleicher (1997) also predicted a stronger dependence on the spectral index than RADYN. These differences may arise for a number of reasons. Chiefly, Ding & Schleicher (1997) used a static code with semiempirical atmospheres and manually varied the temperature and transition region location. The electron beam was only used to add nonthermal collisions, and did not drive the chromospheric response. In our dynamic simulations, while these nonthermal collisions certainly play an important role, their impact on driving the overall dynamics is taken into account, so that there is feedback between the atmosphere and the beam propagation/thermalization.

Recent modeling of LyC emission during solar flares was also performed by Druett & Zharkova (2019) using the radiative-hydrodynamic code, HYDRO2GEN. They present LyC spectra for their 1F10, 1F11, and 1F12 solar flare models with $E_c = 10$ keV. The magnitude of our impulsive phase LyC intensities is in agreement with their spectra. However, the F-CHROMA grid does not include any 1F12 simulations.

3.2. Synthetic LyC Light Curves

The flare excess integrated LyC light curves are shown in Figure 2 for the 3F9, 1F10, 3F10, and 1F11 models, with $E_c = 20$ keV, and spectral indices ranging from $\delta = 3$ –7 (colored lines). Note the saw-toothing seen for some of the

models is due to numerical noise in the spectra between time steps. The synthetic light curves again highlight that the magnitude of the LyC enhancement is primarily driven by the magnitude of the nonthermal electron flux, whereas variations in the spectral index are less significant. Softer beams result in slightly higher LyC fluxes. This is because softer beams (larger δ) deposit their energy over a narrower region in the upper chromosphere, resulting in more localized heating close to the LyC formation region. There is a period of time near the beam onset where the LyC emission is barely enhanced (recall that the flux of the nonthermal electron distribution ramps up in a triangular profile). The duration of this period is dependent upon the flux of the nonthermal electron beam, with larger fluxes having a shorter delay in the enhancement. All models consistently showed that notable LyC enhancement occurred after approximately $3 \times 10^9 - 4 \times 10^9 \text{ erg cm}^{-2}$ of energy was deposited by the beam. Flares that inject larger nonthermal electron fluxes more rapidly produce conditions conducive to LyC ionizations.

Despite this variable onset time, each LyC flare reaches a maximum around $t \sim 10 \text{ s}$ and falls thereafter when the energy flux of the electrons decreases. The LyC response largely tracks the beam heating profile, in agreement with Druett & Zharkova (2019). However, the 1F11, $\delta = 4$, $E_c = 20 \text{ keV}$ model shows a secondary peak in the LyC light curve at $t = 13.6 \text{ s}$. This second maximum occurs as a chromospheric *bubble* (that is, a region of dense, low-temperature material, appearing at high altitude) dissipates at that time, resulting in a decrease in the optical depth (Reid et al. 2020). At the same time, a condensation front producing optically thin LyC emission merges with the heated chromosphere producing the optically thick LyC layer, resulting in a sudden, secondary increase in the LyC intensity. The optically thin LyC layers are discussed in more detail in Section 3.3.

The 1F11, $\delta = 3$, $E_c = 20 \text{ keV}$ and 3F10, $E_c = 20 \text{ keV}$, $\delta = 6$, 7 models also show a secondary increase in LyC emission after the peak beam heating. This is caused by the merging of optically thin condensation fronts with the optically thick LyC layer. However, for these models, the chromospheric bubbles do not dissipate before this merging. For the 1F11, $\delta = 5$, $E_c = 20 \text{ keV}$ model, the merging of the two layers occurs before the peak beam heating, resulting in the peak seen between 9 and 10 s in Figure 2 (the formation layers for this model are discussed in further detail in Section 3.3).

All this is to say that features in the light curves, while largely following the profiles of energy injection, are influenced by the complex dynamics of the flaring chromosphere.

3.3. LyC Formation Properties

3.3.1. Formation Heights and Optical Depth

The contribution function to the emergent intensity effectively shows where in the solar atmosphere the emission originates (for brevity we refer to this simply as the *contribution function* going forward). The formal solution of the emergent intensity can be expressed as

$$I_\lambda = \frac{1}{\mu} \int_z C_I(z) dz = \int_z j_\lambda \exp(\tau_\lambda / \mu) dz, \quad (1)$$

where the integrand is the contribution function, $C_I(z)$ (Magain 1986; Carlsson & Stein 1994). Following Kowalski et al. (2017) we express $C_I(z)$ in terms of emissivity, j_λ ,

attenuated by some optical depth τ_λ . The emissivity and opacities are the sum of various sources, including hydrogen bound-free, hydrogen free-free, H^- , scattering by metals, Rayleigh scattering, and Thomson scattering. Of these, the bound-free transitions are treated fully in NLTE, whereas the others are treated in LTE, but using the NLTE, nonequilibrium electron or proton densities as appropriate (see Kowalski et al. 2017 for more details).

Generally, if the emission originates close to the $\tau_\nu = 1$ surface, then the emission forms under optically thick conditions, and if it originates in a region where $\tau_\nu \ll 1$, then it can be considered to be optically thin. It is possible that some flares may exhibit both optically thick and thin components with significant emission coming from multiple layers, e.g., from an optically thin layer overlying the chromosphere. Knowledge of the plasma properties in the LyC forming region(s), in response to different heating conditions, will broaden our understanding of energy transport processes during flares, and where this energy is deposited.

To illustrate the general formation properties we discuss detailed examples from two simulations: the 3F9, $\delta = 5$, $E_c = 20 \text{ keV}$ and the 1F11, $\delta = 5$, $E_c = 20 \text{ keV}$ models. These showcase a weaker and stronger flare, respectively. Figure 3 shows the temporal evolution of the log of the contribution function for the 3F9, $\delta = 5$, $E_c = 20 \text{ keV}$ model during the heating phase. The temperature stratification (solid red line) and the heights at which $\tau_\lambda = [0.01, 0.1, 1]$ are also indicated (gray dotted-dashed, dashed, and solid lines, respectively). Initially, at $t = 0 \text{ s}$, there is a peak in the contribution function at the base of the transition region ($z \sim 1750 \text{ km}$), forming between $0.1 \lesssim \tau_\lambda \lesssim 1$, corresponding to an optically thick LyC formation, in agreement with the literature (Machado & Noyes 1978; Machado et al. 2018; Druett & Zharkova 2019). By $t = 8 \text{ s}$, the formation region has widened, and shifted deeper into the chromosphere ($z \approx 1200 - 1400 \text{ km}$) as the beam heating strengthens. The height difference between $\tau_\lambda = 1$ for short and long wavelengths has also narrowed. At this time, opacity effects are still significant, with the bulk of the emission forming between $0.1 \lesssim \tau_\lambda \lesssim 1$. A secondary peak in the contribution function is present higher in altitude ($z = 1700 \text{ km}$), cospatial with a chromospheric *bubble*, seen as a narrow dip in the temperature profile forming at the base of the transition region at $t = 8, 10, 14, 18, \text{ and } 20 \text{ s}$ as shown in Figure 3. Emission from this very narrow layer forms under optically thin conditions $\tau_\lambda < 0.01$. Similar regions of cooler, yet dense plasma, are present in most of our simulations (see also Allred et al. 2005; Reid et al. 2020). Druett & Zharkova (2019) also presented evidence for an overlying optically thin layer in their 1F11, $E_c = 10 \text{ keV}$ model. As time progresses, this chromospheric bubble propagates upward toward the corona along a chromospheric ablation (also referred to as *evaporation*) front. The bubble collapses as it propagates, narrowing until all of the cool material has been heated to coronal temperatures (or higher). In the declining phase of the heating ($t > 10 \text{ s}$) the $\tau_\lambda = 1$ layer begins to gradually return to the pre-flare height as the atmosphere cools and the number of recombinations in low opacity regions increases while ionization decreases, in agreement with Druett & Zharkova (2019). The $\tau_\lambda = 0.1$ layer begins shifting to the location of the bubble as the density there increases, raising the LyC opacity at those altitudes.

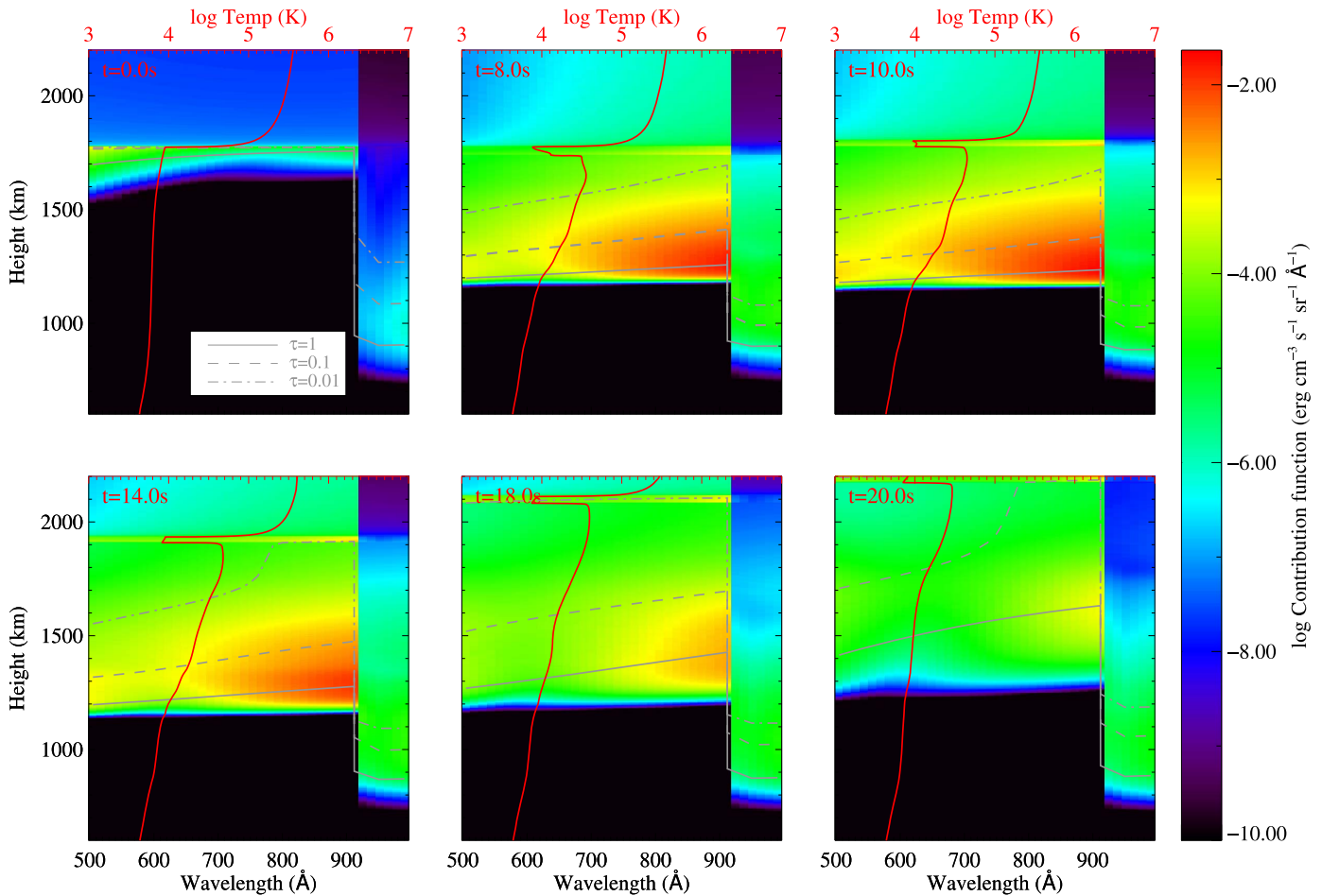


Figure 3. A log of the contribution function for the 3F9, $\delta = 5$, $E_c = 20$ keV model at times $t = [0, 8, 10, 14, 18, 20]$ s. The heights at which $\tau = 1$ (gray solid line), $\tau = 0.1$ (gray dashed line), and $\tau = 0.01$ (gray dotted-dashed line) are shown. The temperature profile is shown in red at each time step.

Figure 4 shows the temporal evolution of the log of the LyC contribution function for the 1F11, $\delta = 5$, $E_c = 20$ keV model during the heating phase. In this more energetic simulation, the LyC forms over much more narrow regions ($z \approx 1000$ – 1100 km) due to the more dramatic response of the chromosphere that becomes very compressed. By $t = 8$ s, two optically thin layers have formed due to bubbles flanking a rapidly expanding high-temperature region (one upflowing bubble due to explosive evaporation at $z \approx 1450$ km, and one downflowing bubble at $z \approx 1250$ km, commonly referred to as chromospheric condensation). When the very dense downflowing bubble effectively merges with the bulk of the chromosphere the density at temperatures favorable to produce LyC can rapidly increase. Since opacity is a strong function of wavelength there can be times at which there is a marked optical depth stratification, resulting in variations to the spectral shape of the LyC (e.g., flattening at certain wavelengths). Examples are shown at $t = [8.8, 11]$ s, where the $\tau_\lambda = 1$ layer forms at a higher altitude for the head of the continuum compared to the tail. In this stronger flare, the chromosphere becomes so compressed that the LyC ultimately forms from a vanishingly narrow downflowing layer in the latter stages of the flare, shown at $t = 15$ s in Figure 4 at $z \approx 1000$ km.

These formation properties are generally true of the other simulations. Most simulations contain some combination of optically thick and overlying optically thin contributions to the emergent spectra (though the bulk of the emission does tend to

originate between $0.1 \lesssim \tau_\lambda \lesssim 1$). Stronger flares produce more dramatic atmospheric responses, leading to bubbles and shocks, and associated phenomena. These dynamics also emerge and develop faster with increasing flare strength, and for softer nonthermal electron distributions. This is because these electrons heat the uppermost chromosphere very efficiently and do not penetrate as deeply, driving flows more easily. Weaker flares and harder spectra do not tend to produce as many shocks, do not significantly compress the chromosphere, and exhibit mainly upflowing features.

3.3.2. Emissivity and Opacity

To understand some of the features described we can briefly look at the components of opacity and emissivity as functions of space, time, and wavelength. We illustrate the components of emissivity and opacity at two times from one flare for long ($\lambda = 900$ Å) and short (700 Å) wavelengths as shown in Figure 5. The dominant source of opacity at all wavelengths, throughout the chromosphere and through the lower transition region was hydrogen free-bound opacity, $\chi_{\lambda, \text{H}_{\text{bf}}}$ (red-dashed line). Toward the upper transition region and corona, where hydrogen is ionized, Thomson scattering begins to dominate but the overall effect on the emerging radiation is small, compared to the free-bound opacity (pink-dashed line).

Once the flare starts in earnest, we saw that the formation height of the LyC dropped in altitude. This is because the upper

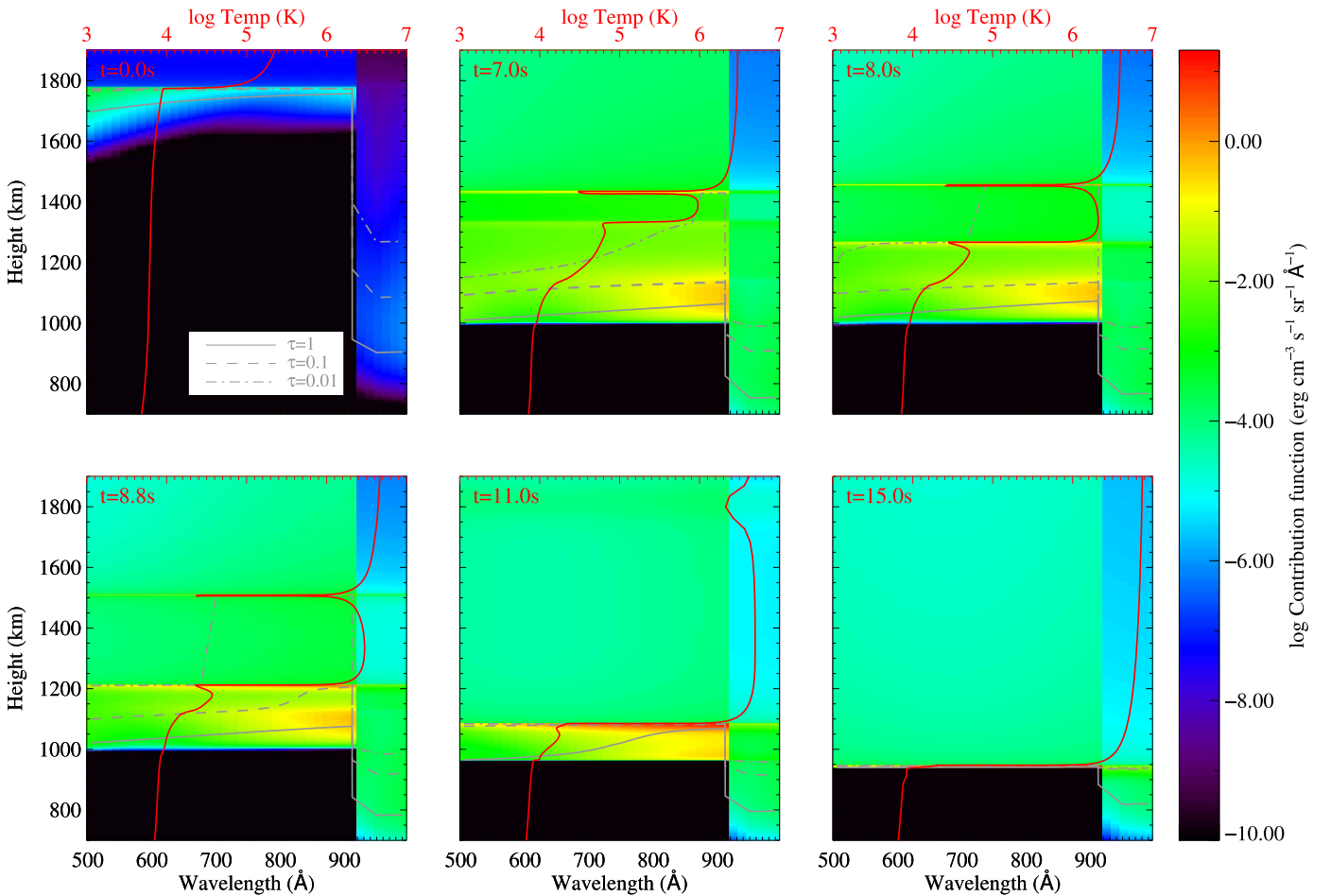


Figure 4. Same as Figure 3, but for the 1F11, $\delta = 5$, $E_c = 20$ keV model. Note the color bar scale has changed.

chromosphere was strongly heated, ionizing hydrogen, and decreasing $\chi_{\lambda, \text{H}_{\text{bf}}}$, meaning that the $\tau_{\lambda} = 1$ forms much deeper in the atmosphere, as shown in the top panels of Figure 5. Later, the merging of the dense bubbles with the bulk of the chromosphere means that $\chi_{\lambda, \text{H}_{\text{bf}}}$ increases, but since this is a function of wavelength, this happens first for longer wavelengths during this process.

The emissivity of the LyC is also dominated by hydrogen recombinations, $j_{\lambda, \text{H}_{\text{bf}}}$ at longer wavelengths (roughly speaking $\lambda > 700$ Å), but at shorter wavelengths, Thomson scattering can be important. Thomson scattering can also compete with $j_{\lambda, \text{H}_{\text{bf}}}$ at longer wavelengths at certain times, but once the electron density is high (e.g., in the narrow chromospheric bubbles) then $j_{\lambda, \text{H}_{\text{bf}}}$ once again dominates. The more extended region of flaring LyC formation compared to the quiet Sun can be understood from the stratification of emissivity and opacity also. During a flare, a greater extent of the chromosphere is at an elevated temperature, and hence electron density, so the free-bound emissivity throughout the greater geometric height range is raised. Integrating over height yields a higher emergent intensity.

In Figure 5, note the initial decrease in opacity (top row $t = 2$ s panels for 700 and 900 Å), pushing LyC formation deeper, and then the influence of the bubbles. The emissivity is largest at the optically thick layer (between $\tau = 0.1$ and 1 heights) as the density of emitting particles is greatest here. The optically thin bubbles also have an increased emissivity

compared to the ambient plasma. At shorter wavelengths the emissivity of the optically thicker layer is comparable to the emissivity of the optically thin bubbles, meaning the optically thin layers will reinforce the lower wavelength LyC intensities to a greater extent than the continuum head, in agreement with the literature (Machado & Noyes 1978; Machado et al. 2018; Druett & Zharkova 2019).

4. LyC Color Temperature and Departure from LTE

4.1. Fitting the LyC Spectra

Following the method used by Machado & Noyes (1978) and Machado et al. (2018), the synthetic LyC spectra were fit using the Eddington–Barbier (EB) relation to determine the values for b_1 and T_c . This approximation equates the emergent intensity to the source function at optical depth unity, and is given by

$$I_{\lambda}(\mu) \approx S_{\lambda}(\tau_{\lambda} = \mu) = \frac{B_{\lambda}(T_c)}{b_1}, \quad (2)$$

where $B_{\lambda}(T_c)$ is the Planck function,

$$B_{\lambda}(T_c) = \frac{2hc^2}{\lambda^5} \frac{1}{\exp\left(\frac{hc}{\lambda k_B T_c}\right) - 1}. \quad (3)$$

I_{λ} is the continuum intensity and S_{λ} is the source function. The λ subscripts indicate that these variables are functions of

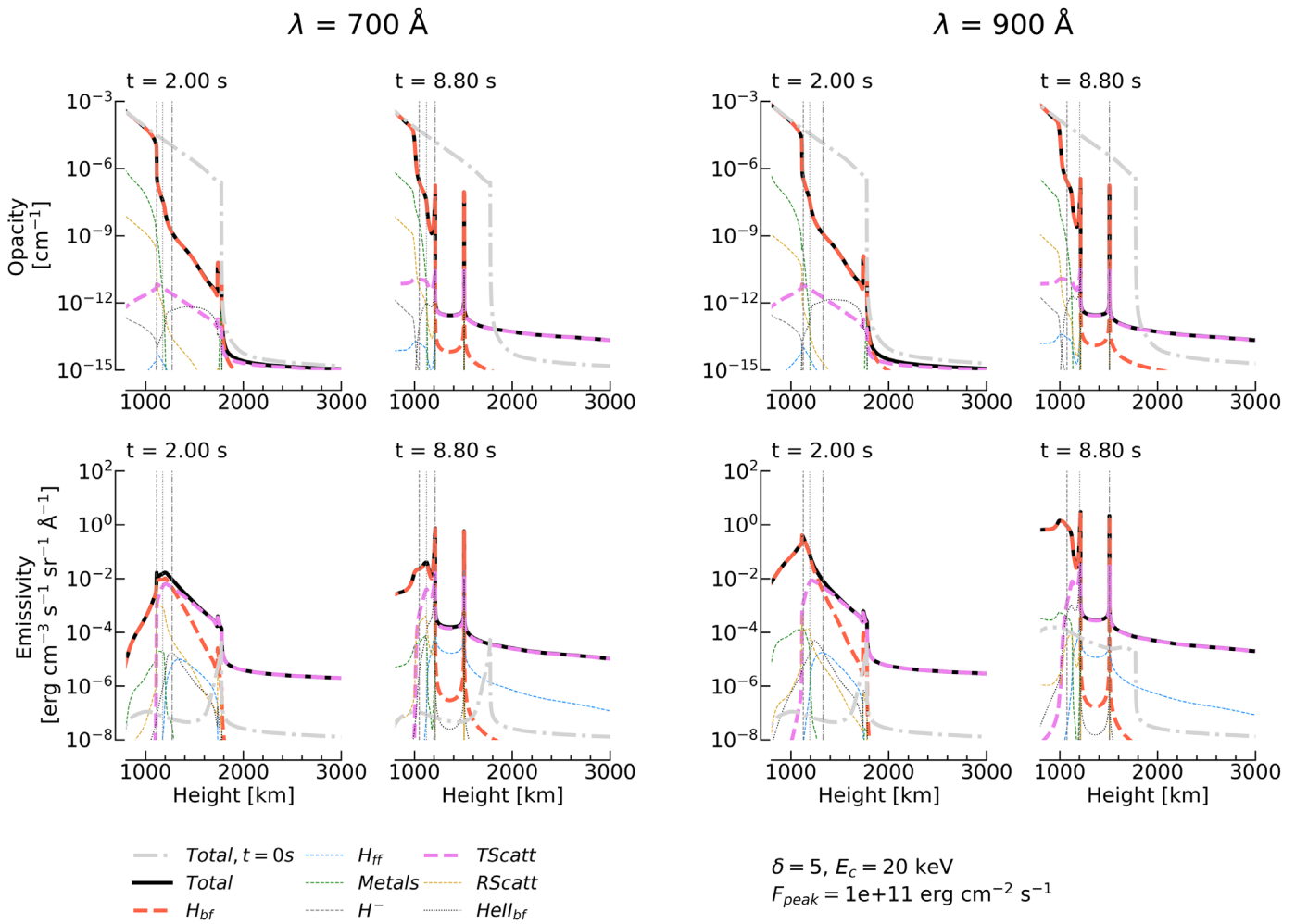


Figure 5. The components of $\lambda = [700, 900]$ Å opacity (top row) and emissivity (bottom row) for two snapshots in the 1F11, $\delta = 5$, $E_c = 20$ keV model. The left-hand panels show 700 Å and the right-hand panels show 900 Å. The light gray dotted–dashed line in each panel shows the total opacity or emissivity at $t = 0$ s. The colored lines correspond to various contributions to the total emissivity or opacity (the sums of these contributions are shown as thick black lines). The vertical lines correspond to the heights at which $\tau = 1$ (dashed), $\tau = 0.1$ (dotted), and $\tau = 0.01$ (dotted–dashed).

wavelength. T_c is the color temperature, b_1 is the nonlocal thermodynamic equilibrium departure coefficient of the first level of hydrogen, and all other constants have their usual meanings.

An illustration of this spectral fitting is shown in the left-hand panel of Figure 6, for various times during the 3F9, $\delta = 5$, $E_c = 20$ keV model. The right-hand panel shows the temporal evolution of the log of the goodness of fit (ϵ) with vertical dashed lines denoting the time of the spectra in the left panel. The goodness-of-fit values are given by

$$\epsilon = \frac{1}{N} \sum_{i=1}^N \frac{|y_i - O_i|}{y_i}, \quad (4)$$

where i is the element index, N is the number of data points, y_i is the data value, and O_i is the fitted value. As the goodness of fit is weighted by the data for each wavelength and time, smaller values correspond to a smaller relative difference between the data and the fit, meaning the fits are better.

As shown in the right-hand panel of Figure 6, at $t \sim 5$ s the beam has mostly heated a region in the atmosphere below the formation height of the LyC (i.e below $\tau_\lambda = 1$, where photons cannot readily escape). As discussed in Section 3.3, the height

at which $\tau_\lambda = 1$ varies with wavelength, typically forming lower in the atmosphere with decreasing wavelength. The difference is a few tens of kilometers at $t = 5$ s. The flare does produce a small increase in emissivity above the height at which $\tau_\lambda = 1$ for shorter wavelengths, increasing the emergent intensity toward the tail of the LyC. At that height, however, $\tau_\lambda > 1$ for the head of the continuum and so there is no meaningful change in the emergent intensity for longer wavelengths. During these times, the LyC spectrum cannot be approximated by the EB assumption, resulting in the large spike in ϵ seen between $t = 5$ – 6 s in the right-hand panel of Figure 6, indicating a poor fit. Further discussion on this behavior can be found in Section 5.2.

In general, the tail of the continuum does not conform to the EB assumption as well as longer wavelengths, particularly in the decay phase following the flare peak. This is due to the presence of the overlying optically thin LyC layers discussed in Section 3.3. When Equation (2) is applied only between $\lambda = 800$ and 911 Å we obtain better fits (the blue line on the goodness-of-fit panel in Figure 6) compared to fitting the full range of $\lambda = 505$ – 911 Å (black line). This suggests two distinct gradients of the LyC, in agreement with the literature (Machado & Noyes 1978; Machado et al. 2018; Druett & Zharkova 2019).

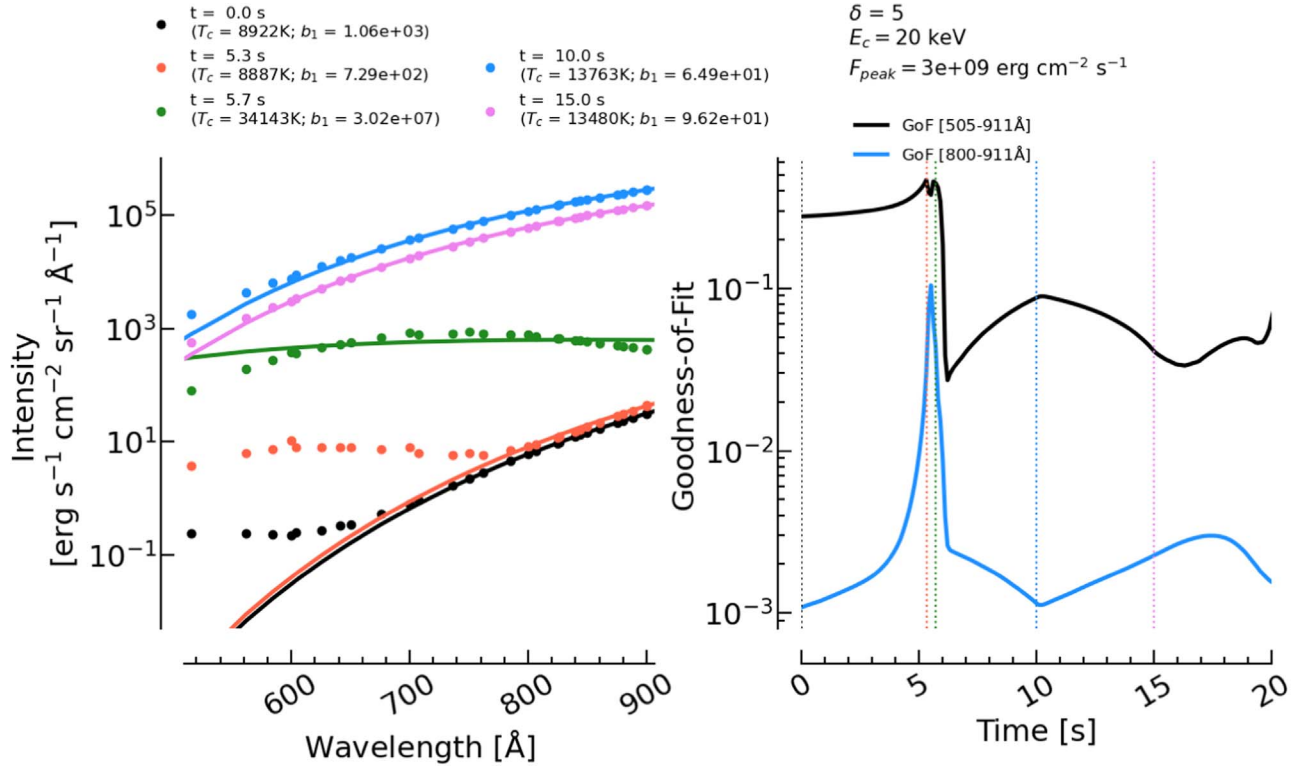


Figure 6. Left-hand panel shows synthetic RADYN spectra from 400–911 Å for the 3F9, $\delta = 5$, $E_c = 20$ keV model, at times $t = 0, 5.3, 5.7, 10,$ and 20 s (colored dots). Fits to LyC using Equation (2) are shown by solid colored lines. The right-hand panel shows the log of the goodness of fit (ϵ) as a function of time for the fits shown in the left panel (solid black curve), while the blue curve illustrates the ϵ values when the data was fit between 800.0 and 911 Å. The dashed colored lines denote the times of the spectra in the left panel.

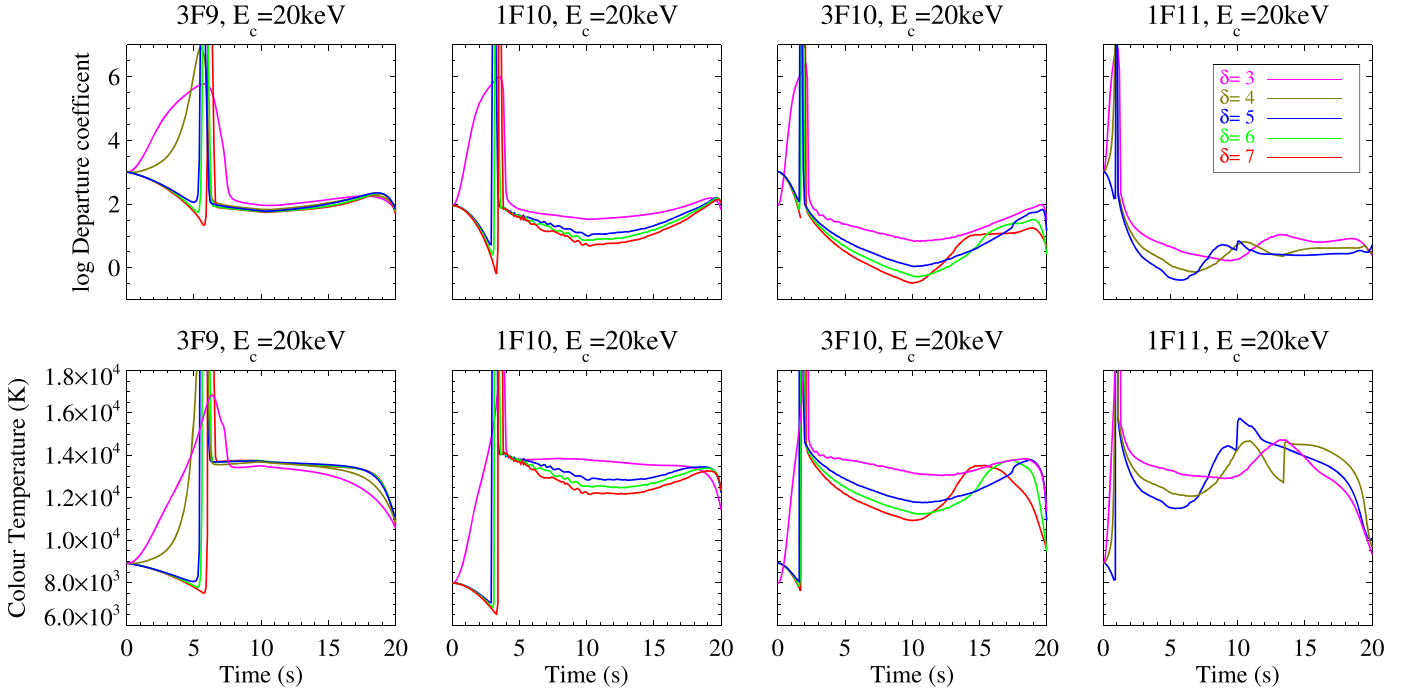


Figure 7. The temporal evolution of b_1 and T_c for the 3F9, 1F10, 3F10, 1F11 models with $E_c = 20$ keV and $\delta = 3-7$.

For times in the simulation where the fit was reasonable, we obtain T_c values consistent with previous studies, increasing from $T_c \sim 9$ to ~ 13.5 kK, with b_1 decreasing, though not reaching unity. Where we see a poor fit (e.g., $t = 5.7$ s) we obtain an exceptionally large b_1 and $T_c > 34$ kK.

Values of T_c and b_1 were obtained by fitting the LyC spectra by applying the EB assumption (Equations (2) and (3)) at each time step from every flare in our study. Figure 7 shows the temporal evolution of b_1 (top row) and T_c (bottom row) for the 3F9, 1F10, 3F10, and 1F11 models, with $\delta = [3-7]$ (colored

lines), and $E_c = 20$ keV where we fit between $\lambda = 700$ and 911 Å. This range was selected as Figure 6 shows that the EB approximation generally fits the data well at those wavelengths, but shorter wavelengths can deviate at certain times.

During the beam onset, the initial response of b_1 and T_c is somewhat dependent on the spectral index. For beams with $\delta \geq 5$, b_1 initially decreases steadily during the beam onset followed by a rapid and sudden increase, whereas beams with $\delta \leq 4$ show an initial gradual increase in b_1 , peaking around the time of the spikes in the other models. We limit the range of the figures to the scales shown, but the b_1 and T_c values at the time of these spikes can be several orders of magnitude larger.

The spikes in b_1 and T_c are caused by the flattening in the continuum head, at which times the EB approximation is no longer a valid assumption; the b_1 and T_c values at these times are unreliable. However, there are three key times when the behavior of b_1 is consistent across all models. At $t = 0$ s, $b_1 \sim 10^2 - 10^3$, decreasing to a minimum around $t \sim 10$ s (flare peak), then increasing again during the decay phase. The magnitude of the b_1 minima depends upon the flux of the nonthermal electron beam: b_1 values for the 3F9 models decrease from $b_1 \sim 10^3$ to $b_1 \sim 10^2$, whereas the 3F10 and 1F11 models decrease closer $10^{-1} < b_1 < 10^1$. The inference there being that more energetic simulations drive LyC formation closer to LTE due to the increased electron densities. Both thermal and nonthermal collisions will significantly increase in those simulations. Ding & Schleicher (1997) presented a similar finding whereby beams with larger nonthermal electron fluxes caused b_1 to decrease to a greater extent.

As discussed earlier, Machado et al. (2018) determined b_1 and T_c values from pre-flare and flaring spectra for the six solar flares they analyzed. The pre-flare fit results from our modeling are consistent with their quiescent T_c and b_1 results. Further, the range of T_c values we measured in our flare simulations is also generally consistent with the observations. During the observed flares, Machado et al. (2018) reported $b_1 \approx 1$, whereas our model results show a wide range of values (between 0.1 and 10^2), depending upon the flux of the nonthermal electron beam. One possible reason for this discrepancy may be due to the dependency of the observed b_1 values scaling with the assumed flaring area. Further details can be found in Machado et al. (2018).

To visualize the spread of the T_c and b_1 values we produced a 2D histogram that collates the information from all simulations for all times with parameters $\delta = [3, 4, 5]$, $E_c = [15, 20, 25]$ keV, $F_{\text{peak}} = [3F9, 1F10, 3F10, 1F11]$ erg s⁻¹ cm⁻² (recall that the $F_{\text{peak}} = 1F11$ simulations did not include the $E_c = 15$ keV scenario). This is shown in Figure 8, where it is clear that T_c increases from quiet-Sun values, $T_c \sim 8-9$ kK, to values roughly in the range of $T_c \sim 10-16$ kK, in agreement with the literature (Machado & Noyes 1978; Ding & Schleicher 1997; Lemaire et al. 2004; Machado et al. 2018). There are two distinct clusters within the histogram; the cooler cluster ($T_c \sim 6-11$ kK, $b_1 \sim 10^1-10^5$) and the hotter cluster ($T_c \sim 10-20$ kK, $b_1 \sim 10^1-10^3$). The cooler cluster corresponds to times before the brief breakdown in the EB approximation, while the hotter cluster corresponds to times after this.

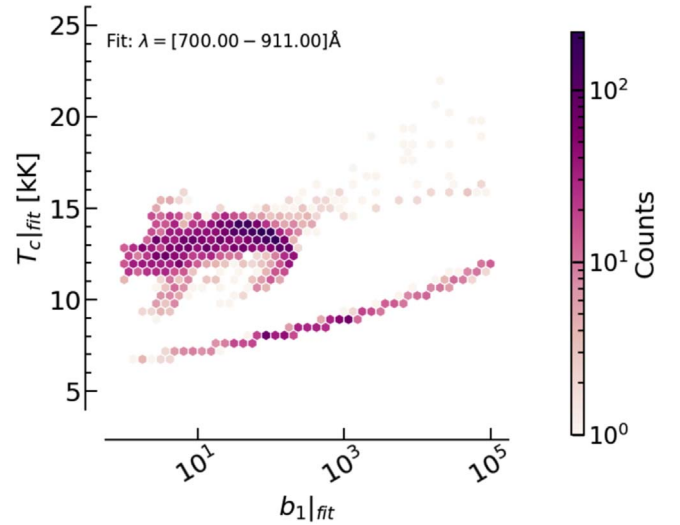


Figure 8. Histogram of T_c and b_1 obtained from fitting the EB approximation to our simulation grid, weighted by the number of counts.

4.2. Comparison of Spectral Fitting to Derived Plasma Properties

We can assess how consistent the properties derived from fitting the spectra are with the actual plasma conditions in the models by comparing the b_1 values directly from RADYN, which we refer to as $b_{1,\text{rad}}$. The atomic level populations are functions of height and wavelength, and so to obtain $b_{1,\text{rad}}$ averaged over the LyC formation region we calculate the normalized cumulative distribution function (NCDF) of the contribution function, C_{cdf} (see also, e.g., Kowalski et al. 2017). The heights corresponding to where the bulk of the emission originates are selected. The weighted average of $b_{1,\text{rad}}$ in that formation region was then obtained, weighted by the contribution function

$$\langle b_{1,\text{rad}} \rangle = \frac{\int_{z(C_{\text{cdf}}=\text{low}})}^{z(C_{\text{cdf}}=\text{upp})} C_I(z) b_{1,\text{rad}} dz}{\int_{z(C_{\text{cdf}}=\text{low}})}^{z(C_{\text{cdf}}=\text{upp})} C_I(z) dz}, \quad (5)$$

where $z(C_{\text{cdf}}=\text{low})$ refers to the height at which the C_{cdf} reaches the lower bound, and $z(C_{\text{cdf}}=\text{upp})$ the height of the upper bound; for example, the heights corresponding to 10% and 90% of the C_{cdf} , respectively.

Figure 9 shows $\langle b_{1,\text{rad}} \rangle$ compared with b_1 obtained from our spectral fitting (solid black line). Formation height ranges corresponding to [10%–90%, 50%–90%, 10%–40%] (red, blue, and purple lines, respectively) were considered. These ranges were selected by integrating the contribution function as a function of height and determining the ranges where the emission became optically thick or thin. The emission range of 10%–90% considers both optically thick and thin components, 50%–90% considers emission between $\tau_\lambda \approx 0.1$ and 1 (optically thick), and 10%–40% considers emission above the $\tau_\lambda < 0.1$ layer (optically thin) at 900.3 Å. The $\langle b_{1,\text{rad}} \rangle$ values from the optically thick layer are more consistent with those obtained from the spectra but deviate during the declining phase of the beam heating.

The $\langle b_{1,\text{rad}} \rangle$ values determined over 10%–90% and 10%–40% of the NCDF are significantly larger than the values determined from the spectra. The former represents an assessment of what the $\langle b_{1,\text{rad}} \rangle$ value when including both

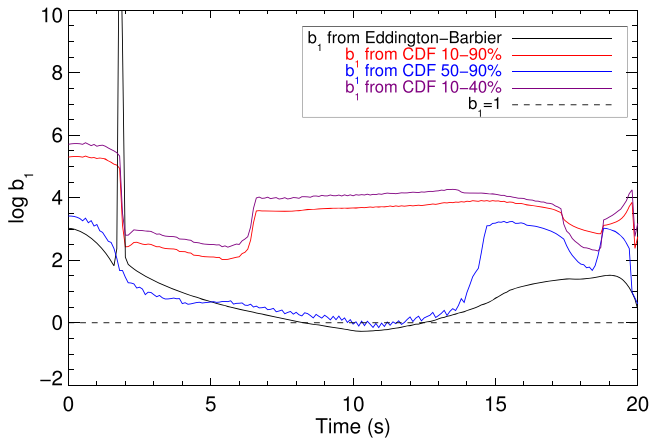


Figure 9. Temporal evolution of $\langle b_{1,\text{rad}} \rangle$ values for the 3F10, $\delta = 6$, $E_c = 20$ keV model. The $\langle b_{1,\text{rad}} \rangle$ values are shown for where $\lambda = 900.3$ Å emission originates, considering $C_{\text{cdf}} = [10\%–90\%, 50\%–90\%, 10\%–40\%]$ (red, blue, and purple, respectively). Also shown is the result of fitting the spectra between $\lambda = 700$ and 911 Å using the EB approximation (solid black line). The $b_1 = 1$ line is shown by the dashed black line for reference.

thick and thin LyC emitting regions. This suggests that the thin components (originating from the bubbles) have such large $\langle b_{1,\text{rad}} \rangle$ values that they drag the overall average up considerably from the values in the chromosphere. The fact that $\langle b_{1,\text{rad}} \rangle$ derived from the optically thick region is more consistent with b_1 derived from spectral fitting could be due to the optically thick emission dominating the emergent intensity.

In a similar manner, the average electron temperature, $\langle T_e \rangle$ from the LyC forming regions was calculated (replacing $b_{1,\text{rad}}$ for T_e in Equation (5)). As b_1 tends toward unity, T_c is expected to tend toward the electron temperature, T_e (Machado et al. 2018). Figure 10 shows the ratio of T_c to $\langle T_e \rangle$, determined when b_1 is at a minimum for the 3F9, 1F10, 3F10, and 1F11 models, with $\delta = 5–7$ and $E_c = 20$ keV outside of the times of the anomalous b_1 values. $\langle T_e \rangle$ was determined over the optically thick layer (50%–90% of the C_{cdf}) as the $\langle b_{1,\text{rad}} \rangle$ values over this emission range are in general agreement with the b_1 values obtained from the fits at these times. From Figure 10, it can be seen that the ratio of T_c to $\langle T_e \rangle$ is clustered around 1 when b_1 reaches a minimum. The minimum b_1 has a rather large range, extending from $b_1 < 1$ to ~ 100 . That is, the ratio $T_c : \langle T_e \rangle$ approaches unity at the minimum value of b_1 but b_1 itself does not necessarily have a value of unity, somewhat contrary to our expectations. Machado et al. (2018) present a similar finding where the six different X-class flares they observed had varying b_1 values ($b_1 < 1$ to $b_1 \sim 68$). However, as they used EVE Sun-as-a-star observations, they converted EVE spectral irradiances to specific intensities by assuming the flaring area. Machado et al. (2018) assumed a fixed flaring area of 10^{18} cm^{-2} , representing the middle of a rather large range of reported areas of X-class flares (see Section 4 of Machado et al. 2018). Varying this area would in effect shift the LyC-specific intensity up or down, while keeping the spectral slope fixed. This would vary the b_1 value but not T_c .

Outside of the times when b_1 is at a minimum, the ratio of T_c to T_e was found to have a large range of values. Figure 11 shows the ratio of T_c to T_e as a function of b_1 for all models, weighted by time. As seen in Figure 11, even as b_1 approaches unity, the range of T_c/T_e extends from 0.1–1.5. This may be

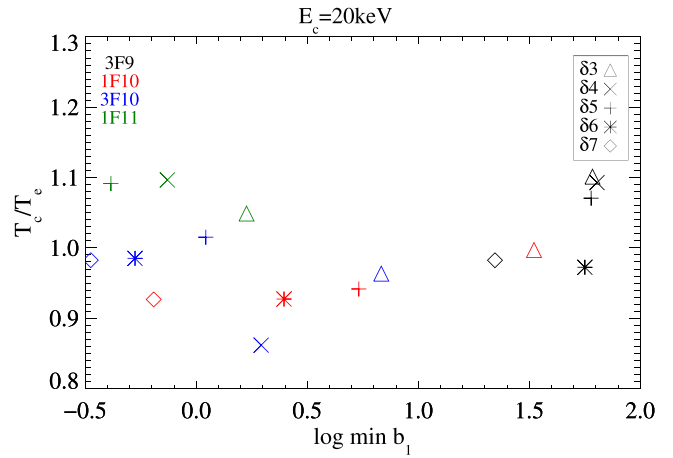


Figure 10. The ratio of T_c to the electron temperature (T_e), determined when b_1 is at a minimum, for the 3F9, 1F10, 3F10, and 1F11 models, with $\delta = 3–7$, and $E_c = 20$ keV where available. T_e was determined from RADYN for emission between 50% and 90% of the normalized contribution function at 900.3 Å. T_c and b_1 values were determined from fitting the spectra between 700.0 and 911.0 Å.

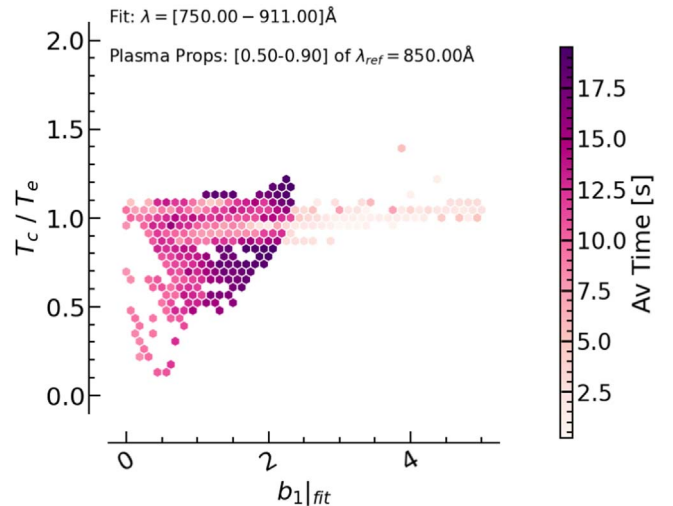


Figure 11. The ratio of T_c to electron temperature (T_e) as a function of b_1 for all models, weighted by time. T_e was determined from RADYN for emission between 50% and 90% of the normalized contribution function at 850.0 Å. T_c and b_1 values were determined by fitting the spectra between 750.0 and 911.0 Å.

because $\langle T_e \rangle$ is determined using the NCDF of the contribution function. As $\langle T_e \rangle$ is determined over a given emission range, the heights considered will vary from model to model, particularly for the more energetic beams where the dynamics of the formation layers occur on shorter timescales (see Figures 3 and 4). Therefore, the value of $\langle T_e \rangle$ is dependent on the height range considered.

Finally, we determined $\langle T_e \rangle$ and $\langle n_e \rangle$ for $\lambda = 850$ Å to illustrate the general range of plasma properties where LyC forms. Those are presented as a 2D histogram in Figure 12 in which properties from $\delta = [3, 4, 5]$, $E_c = [15, 20, 25]$ keV, $F_{\text{peak}} = [3F9, 1F10, 3F10, 1F11]$ $\text{erg s}^{-1} \text{ cm}^{-2}$ were collated. Figure 12 shows that while there is some spread to high temperatures (due mostly to contributions from dense, optically thin bubbles) the bulk of the flare emission forms in the range $\langle T_e \rangle = 10–30$ kK, with electron densities spanning $\langle n_e \rangle = 10^{11–14} \text{ cm}^{-3}$. The data has been weighted by the average

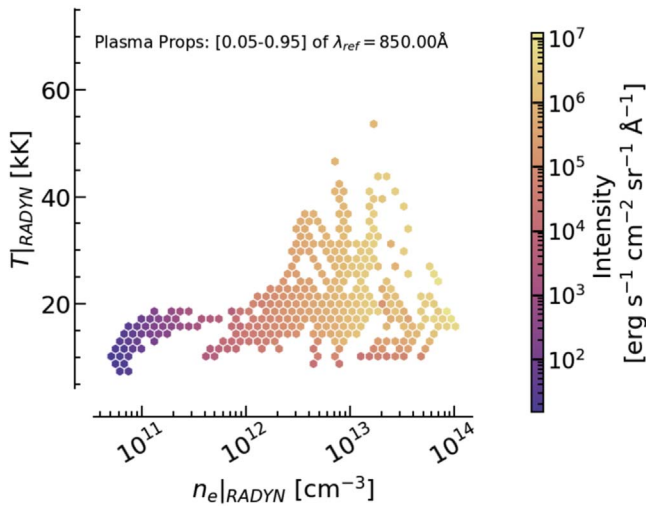


Figure 12. Histogram of $\langle T_e \rangle$ and $\langle n_e \rangle$ in the formation region of $\lambda = 850 \text{ \AA}$, weighted by the average intensity of the emission.

intensity of emission, and indicates that higher intensity is generally associated with higher $\langle n_e \rangle$, though temperature also plays a role.

5. Discussion

5.1. Percentage of Energy Radiated Away by the LyC

To determine the percentage of energy radiated by the LyC compared to the total energy injected via nonthermal electrons, the LyC light curves in Figure 2 were integrated over time and divided by the total nonthermal electron energy. We found the LyC radiated away between 1% and 3% of the total nonthermal electron energy injected. The 3F9 models radiated away around 1% of the total injected energy through the LyC, whereas the 3F10 models radiated around 3%. The overall distribution from a number of simulations is shown in Figure 13.

Milligan et al. (2014) provided a study of the global energy budget in a strong flare, comparing the energy radiated in the lower solar atmosphere at optical, UV, and EUV wavelengths to the energy injected via nonthermal electrons. They found the LyC radiated away approximately 1% of the total nonthermal electron energy. This is in agreement with our findings that predict LyC to radiate away a few percent of the total nonthermal electron energy.

5.2. Spikes in the Departure Coefficient and Color Temperature Values

We mentioned several times previously the appearance of strong spikes in b_1 and T_c , caused by a flattening toward the head of the LyC, as seen, for example, at $t = 5.7 \text{ s}$ in the left-hand panel of Figure 6. The EB approximation is clearly no longer valid during these times.

This phenomenon can be understood from Figure 14, which shows the temporal evolution of the ground state of the hydrogen level population for the 3F9 models, with $E_c = 20 \text{ keV}$, and $\delta = [3, 5]$. The height of the peak of the LyC contribution function is shown by the vertical dashed lines at each time step. At $t = 0 \text{ s}$, n_1 is large in the chromosphere and decreases across the transition region for both models. As the beam heating begins, n_1 decreases within the chromosphere due to excitation and ionization

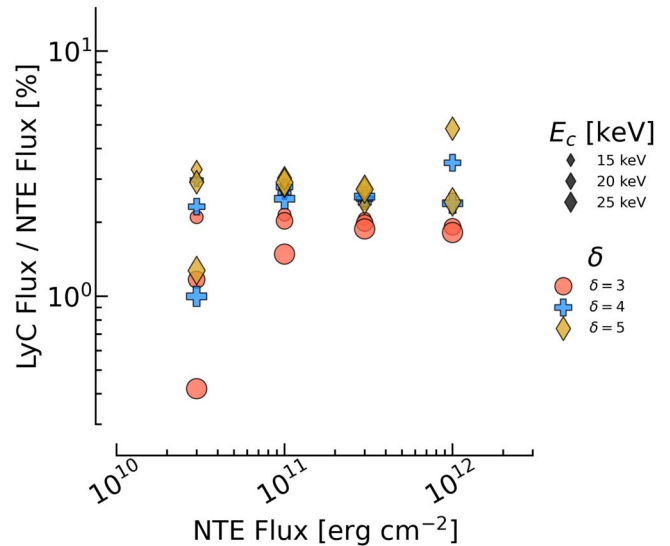


Figure 13. The ratio of energy radiated by LyC to the energy injected by nonthermal electrons (NTEs), as a function of the nonthermal electron energy. Circles represent $\delta = 3$, plus symbol $\delta = 4$, and diamonds $\delta = 5$. The symbols increase in size with increasing E_c .

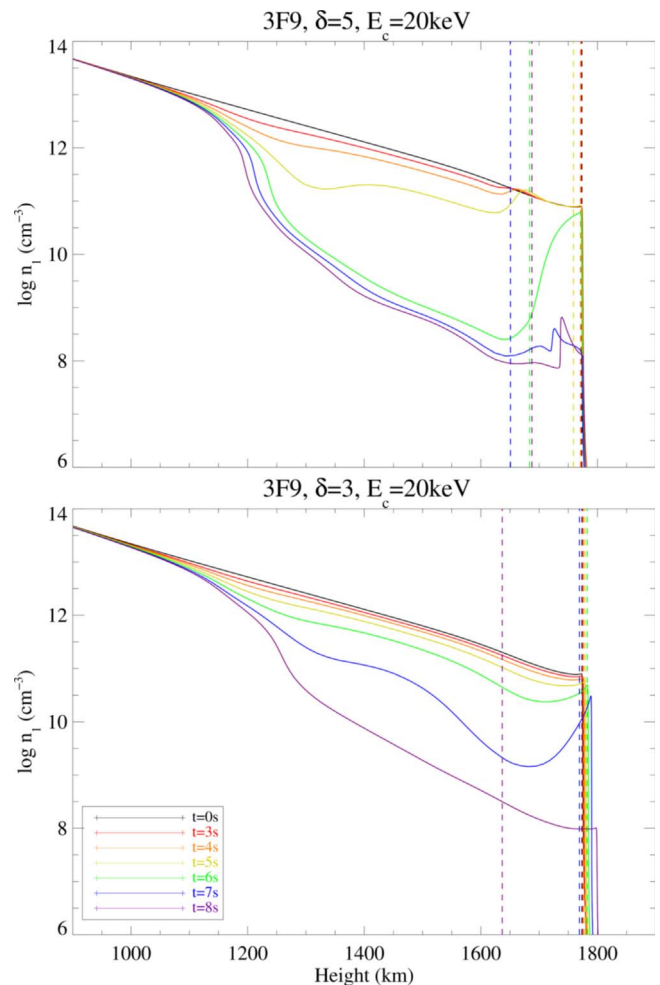


Figure 14. The temporal evolution of the ground state of hydrogen level population for the 3F9 models, with $E_c = 20 \text{ keV}$, and $\delta = [3, 5]$. The height of the peak of the LyC contribution function is shown by the vertical dashed lines at each time step.

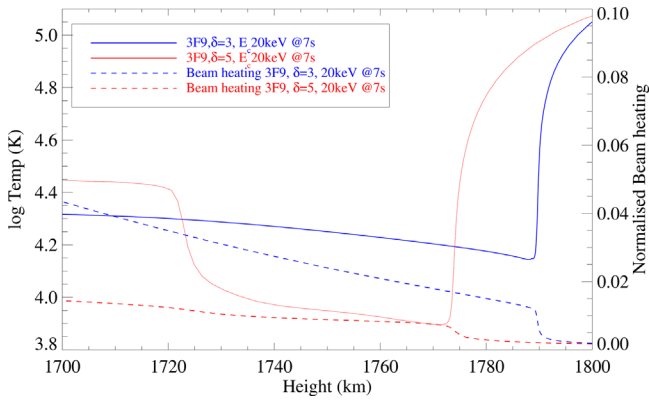


Figure 15. Temperature profiles for the 3F9 models, with $E_c = 20$ keV, and $\delta = 3$ and 5 at $t = 7$ s. The normalized beam heating is shown by the dashed lines for both models.

following the temperature increase and nonthermal collisions. However, there is a small region of plasma between the beam heating region and the transition region that is only minimally heated by the nonthermal electrons, resulting in n_1 remaining large compared to the adjacent plasma. At later times, the optically thick layer shifts much deeper into the chromosphere. The photons emitted from the optically thick layer subsequently get absorbed by this region of plasma, resulting in the flattening of the head of the LyC, and the delayed enhancement of the LyC light curves. For the $\delta = 3$ model, the optically thick layer of the LyC forms below the region of minimal heating for a few seconds until the region dissipates, resulting in the extended increase in b_1 and T_c observed for harder beams (see $\delta = 3-4$ curves in Figure 7). Whereas for softer beams (see $\delta \geq 5$ curves in Figure 7), the optically thick layer only forms below the region of minimal heating for a shorter duration, resulting in the sudden steep spikes in b_1 and T_c .

In Figure 14, the n_1 values for the harder beam ($\delta = 3$) are reduced more uniformly and at higher altitudes within the chromosphere despite harder beams being composed of a greater number of high-energy, deeply penetrating, electrons. This can be understood from Figure 15, which shows the temperature and beam heating profile for the 3F9 models, with $E_c = 20$ keV, and $\delta = 3$ (harder beam; blue lines) and 5 (softer beam; red lines). The region of minimal heating is thicker for softer beams ($z \approx 1720-1770$ km). The $\delta = 3$ beam is harder and therefore has a greater number of high-energy electrons, which results in a faster atmospheric response and evaporation of chromospheric plasma. As the evaporation front propagates the mass density of the upper atmosphere is increased by approximately a few orders of magnitude. The increased column depth means that the higher energy electrons in the $\delta = 3$ beam are thermalized higher up in the atmosphere at later times in the simulation despite the $\delta = 5$ beam being composed of more low-energy electrons, as can be seen by the blue- and red-dashed lines in Figure 15. This results in the narrower region of minimal heating ($z \approx 1790$ km) seen for the harder $\delta = 3$ case. The thickness of this region also contributes to the varying profiles during the sudden increases (spikes) in b_1 and T_c .

5.3. Wavelength Dependency of b_1 and T_c

Machado & Noyes (1978) hypothesized from observational evidence that a higher-lying region contributes an optically thin

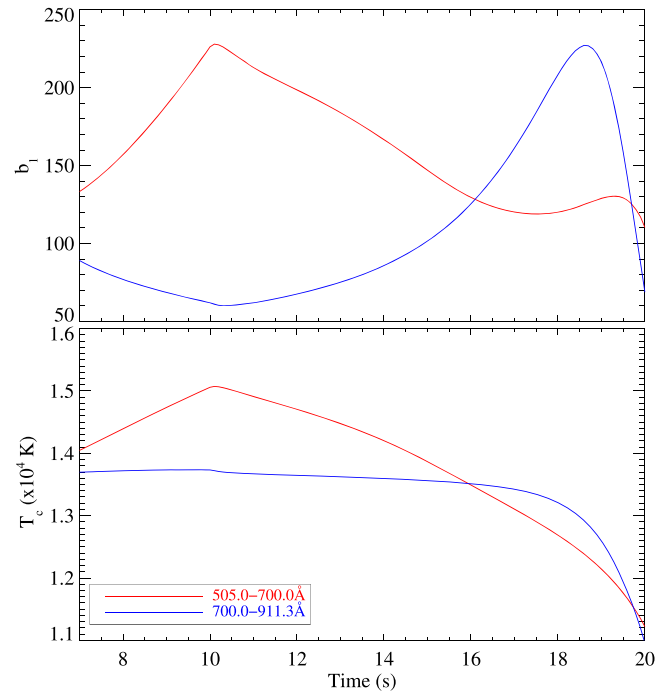


Figure 16. Evolution of b_1 and T_c for the 3F9, $\delta = 5$, $E_c = 20$ keV model. Equations (2) and (3) have been applied between $\lambda = [505-700]$ Å and $\lambda = [700-911]$ Å. The values are only shown between $t = [7$ and $30]$ s to omit times where we know that spectral fitting produced poor results.

component to the LyC during flares alongside the bulk of the chromospheric emission. Evidence for this optically thin layer comes from a steepening in the LyC spectrum's gradient away from the continuum head, resulting in increased T_c values determined at shorter wavelengths. As shown in the right-hand panel of Figure 6, there is a local peak in ϵ at $t = 10$ s. Shorter wavelengths, between $\lambda \sim 505.0$ and 700.0 Å, are poorly fit compared to longer wavelengths. This spectrum has two distinct gradients, one at shorter wavelengths, $\lambda \leq 700$ Å, and the other at longer wavelengths, $\lambda \geq 700$ Å, in agreement with Machado & Noyes (1978), Machado et al. (2018), and Druett & Zharkova (2019).

Figure 16 shows the b_1 and T_c values for the 3F9, $\delta = 5$, $E_c = 20$ keV model, where the EB approximation has been applied between $\lambda = 505-700$ Å and $\lambda = 700-911$ Å. Generally, the T_c values determined at shorter wavelengths were a few thousand Kelvin hotter than at longer wavelengths, in agreement with the literature (Machado & Noyes 1978; Machado et al. 2018). The b_1 values are also generally larger at shorter wavelengths. This is due to the optically thin components of the LyC that enhance the spectrum at shorter wavelengths. The number of optically thin components that form depends on the type of evaporation observed. Gentle evaporation resulted in one upwardly propagating optically thin layer forming. Whereas, explosive evaporation resulted in two or three optically thin components corresponding to evaporation and condensation fronts. The upward propagating optically thin components of the LyC in Figure 4 are due to bubbles of chromospheric material traveling immediately ahead of the evaporation front.

Reid et al. (2020) state that these bubbles are a source of optically thin Ca II 8542 Å line emission and do not always emit strongly in the H α line, while Brown et al. (2018) found solar bubbles to be among the dominant sources of Ly α line

emission. Such propagating high-density features could be indirectly detected via LyC observations due to the effect they have on the spectral shape, manifesting as an increase in both T_c and b_1 at shorter wavelengths. Machado et al. (2018) only observed an increase in T_c at shorter wavelengths for one of the six events that they analyzed. This may be due to the fact that the other five flares did not provide the correct conditions for a solar bubble to form, or at the time of observation the bubbles had dissipated.

6. Conclusions

Using the F-CHROMA grid of RADYN models, we have shown that the LyC is greatly enhanced during solar flares. The LyC spectral response is highly sensitive to the flux of the nonthermal electron beam, but is less dependent upon the spectral index or low-energy cutoff. LyC was found to radiate away between 1% and 3% of the total nonthermal electron energy injected. Increases in solar irradiance associated with solar flares are known to drive dynamic and compositional changes in Earth's ionosphere, which can have adverse implications for modern technology on which society has become dependent. The 850–1027 Å range, in particular, is absorbed at an altitude of around 105–120 km in the ionosphere (E-layer), where it drives the partial dissociation of molecular oxygen (Robinson 1959). This part of the spectrum is dominated by LyC, along with higher-order Lyman emission lines.

Both optically thin and thick layers of the LyC were found to form during solar flares, in agreement with the literature (Machado & Noyes 1978; Machado et al. 2018; Druett & Zharkova 2019). The optically thick layer is formed in NLTE in the QS and forms at the top of the chromosphere. During solar flares, this layer shifts deeper into the solar chromosphere due to the evaporation of the upper chromosphere, forming near the peak beam heating region, with $\langle T_e \rangle \approx 10\text{--}40$ kK. It also forms closer to LTE conditions. The optically thin components of the LyC formed due to chromospheric evaporation, with the number of optically thin components forming being dependent on the type of evaporation observed, gentle or explosive. These optically thin components cause an enhancement in intensities away from the LyC head, resulting in increased b_1 and T_c values determined at shorter wavelengths. Fitting with the EB relation we find that $T_c \approx 10\text{--}16$ kK, with b_1 at times dropping to $b_1 \approx \text{few} \times 10$, but which have a large scatter.

Our results suggest that the LyC spectral response is indicative of a chromospheric temperature and density enhancement largely probing the chromosphere. Gradients in the derived T_c as a function of wavelength can also indicate the presence of regions of propagating dense, cool material in the upper atmosphere. The number of optically thin layers formed was found to be greater for stronger solar flares, and the LyC contribution functions presented show that the optically thin layers form and dissipate over a shorter period for stronger flares. Model-data discrepancies (e.g., the large scatter of b_1 values that do not always approach unity, contrary to Machado et al. 2018), could result from an exaggerated optically thin component to the LyC forming in the dense bubbles, if those bubbles are denser than in actual flares. For example, Graham et al. (2020) modeled the ratio of the intensity of redshifted *satellite* components of the Fe II line to the intensity of the stationary component, noting that it was larger than the

observed flare they were simulating. This could be due to the density in the modeled condensation (from which the satellite component originated) being larger than the condensation produced during the observed flare. Our chromospheric bubbles may be similarly over-dense.

EVE currently provides LyC observations with the greatest coverage. However, these are Sun-as-a-star observations with a cadence of 60 s (observations prior to 2014 had a 10 s cadence, but instrument degradation has forced a longer exposure time). Therefore, EVE LyC flare observations will observe a range of flaring loops at various heating or cooling stages. Thus, some of the dynamic features may become smeared temporally, especially for stronger flares. As the breakdown in the EB approximation and delayed enhancement in the LyC light curves also occur over second to sub-second timescales, it is unlikely that EVE can observe these phenomena. Additionally, as EVE provides Sun-as-a-star observations, EVE spectral irradiances can be converted to specific intensities by assuming the flaring area as discussed in Section 4.2. Varying this area shifts the LyC-specific intensity up or down, while keeping the spectral slope fixed. This would vary the b_1 value but not T_c .






SPICE on board the Solar Orbiter mission, which was launched in 2020, provides EUV coverage in the wavelength ranges of $\lambda = 704\text{--}790$ Å and $\lambda = 973\text{--}1049$ Å. This provides partial coverage of LyC. It remains to be seen to what extent it is possible to extract continuum intensities, which will depend in part on how well we can resolve spectral lines with that passband, but SPICE observations may be used to determine b_1 and T_c values below the head of the LyC. Unlike SDO/EVE, these observations would have spatial resolution and obtain higher cadences. However, as SPICE only provides partial coverage of LyC, the derived b_1 and T_c values may be elevated due to the presence of the optically thin LyC layers, enhancing the LyC spectrum at shorter wavelengths. To determine if this is the case, b_1 and T_c values should be derived and compared from SPICE and EVE spectra over multiple wavelength ranges for any flares both instruments capture. Our analysis paves the way for an interpretation of solar flare LyC observations taken by current and future missions.

We thank the anonymous referee for a careful review of our manuscript, and for useful comments and suggestions. S.A.M. would like to thank the Science and Technology Facilities Council (UK) for the award of a PGR studentship. A.J.M. acknowledges funding from the Science Technology Funding Council (STFC) Grant Code ST/T506369/1. R.O.M. and G.S.K. would like to acknowledge support from NASA Heliophysics Supporting Research grant NNH19ZDA001N and R.O.M. thanks the Science and Technologies Facilities Council (UK) for the award of an Ernest Rutherford Fellowship (ST/N004981/2). P.J.A.S. acknowledges support from the Fundo de Pesquisa Mackenzie (MackPesquisa), CNPq (contract 307612/2019-8), and FAPESP, the Sao Paulo Research Foundation (contract 2013/24155-3). G.S.K. thanks Dr. Adam Kowalski for sharing some analysis software that was adapted to perform this work.

Data Access Statement

No new data were generated during the research for this paper. The pre-existing data analyzed are available at <https://star.pst.qub.ac.uk/wiki/public/solarmodels/start.html>

ORCID iDs

Shaun A. McLaughlin  <https://orcid.org/0000-0002-6900-0936>
 Ryan O. Milligan  <https://orcid.org/0000-0001-5031-1892>
 Graham S. Kerr  <https://orcid.org/0000-0001-5316-914X>
 Aaron J. Monson  <https://orcid.org/0000-0002-3305-748X>
 Paulo J. A. Simões  <https://orcid.org/0000-0002-4819-1884>
 Mihalis Mathioudakis  <https://orcid.org/0000-0002-7725-6296>

References

- Abbett, W. P., & Hawley, S. L. 1999, *ApJ*, 521, 906
 Allred, J. C., Alaoui, M., Kowalski, A. F., & Kerr, G. S. 2020, *ApJ*, 902, 16
 Allred, J. C., Hawley, S. L., Abbett, W. P., & Carlsson, M. 2005, *ApJ*, 630, 573
 Allred, J. C., Kowalski, A. F., & Carlsson, M. 2015, *ApJ*, 809, 104
 Arnaud, M., & Rothenflug, R. 1985, *A&AS*, 60, 425
 Avrett, E. H., & Loeser, R. 2008, *ApJS*, 175, 229
 Brown, J. C. 1971, *SoPh*, 18, 489
 Brown, S. A., Fletcher, L., Kerr, G. S., et al. 2018, *ApJ*, 862, 59
 Carlsson, M., & Stein, R. F. 1994, in Proc. Mini-workshop on Chromospheric Dynamics, ed. M. Carlsson (Oslo), 47
 Carlsson, M., & Stein, R. F. 1992, *ApJL*, 397, L59
 Carlsson, M., & Stein, R. F. 1995, *ApJL*, 440, L29
 Carlsson, M., & Stein, R. F. 1997, *ApJ*, 481, 500
 Ding, M. D., & Schleicher, H. 1997, *A&A*, 322, 674
 Domingo, V., Fleck, B., & Poland, A. I. 1995, *SoPh*, 162, 1
 Dorfi, E. A., & Drury, L. O. 1987, *JCoPh*, 69, 175
 Druett, M. K., & Zharkova, V. V. 2018, *A&A*, 610, A68
 Druett, M. K., & Zharkova, V. V. 2019, *A&A*, 623, A20
 Fang, C., Henoux, J. C., & Gan, W. Q. 1993, *A&A*, 274, 917
 Fletcher, L., Dennis, B. R., Hudson, H. S., et al. 2011, *SSRv*, 159, 19
 Graham, D. R., Cauzzi, G., Zangrilli, L., et al. 2020, *ApJ*, 895, 6
 Holman, G. D., Sui, L., Schwartz, R. A., & Emslie, A. G. 2003, *ApJL*, 595, L97
 Holman, G. D., Aschwanden, M. J., Aurass, H., et al. 2011, *SSRv*, 159, 107
 Ise, R., & Cagle, E. H. 1974, *AcAau*, 1, 1315
 Karlicky, M., Kasparova, J., & Heinzel, P. 2004, *A&A*, 416, L13
 Kasparova, J., Varady, M., Heinzel, P., Karlicky, M., & Moravec, Z. 2009, *A&A*, 499, 923
 Kennedy, M. B., Milligan, R. O., Allred, J. C., Mathioudakis, M., & Keenan, F. P. 2015, *A&A*, 578, A72
 Kerr, G. S., Allred, J. C., & Polito, V. 2020, *ApJ*, 900, 18
 Kerr, G. S., Carlsson, M., Allred, J. C., Young, P. R., & Daw, A. N. 2019, *ApJ*, 871, 23
 Kerr, G. S., Fletcher, L., Russell, A. J. B., & Allred, J. C. 2016, *ApJ*, 827, 101
 Kerr, G. S., Xu, Y., Allred, J. C., et al. 2021, *ApJ*, 912, 153
 Kontar, E. P., Brown, J. C., Emslie, A. G., et al. 2011, *SSRv*, 159, 301
 Kontar, E. P., Dickson, E., & Kasparova, J. 2008, *SoPh*, 252, 139
 Kowalski, A. F., & Allred, J. C. 2018, *ApJ*, 852, 61
 Kowalski, A. F., Allred, J. C., Carlsson, M., et al. 2022, *ApJ*, 928, 190
 Kowalski, A. F., Allred, J. C., Daw, A., Cauzzi, G., & Carlsson, M. 2017, *ApJ*, 836, 12
 Kowalski, A. F., Hawley, S. L., Carlsson, M., et al. 2015, *SoPh*, 290, 3487
 Krucker, S., Kontar, E. P., Christe, S., & Lin, R. P. 2007, *ApJL*, 663, L109
 Krucker, S., Saint-Hilaire, P., Christe, S., et al. 2008, *ApJ*, 681, 644
 Lemaire, P., Gouttebroze, P., Vial, J.-C., et al. 2004, *A&A*, 418, 737
 Lin, R. P., Dennis, B. R., Hurford, G. J., et al. 2002, *SoPh*, 210, 3
 Machado, M. E., Milligan, R. O., & Simoes, P. J. A. 2018, *ApJ*, 869, 63
 Machado, M. E., & Noyes, R. W. 1978, *SoPh*, 59, 129
 Magain, P. 1986, *A&A*, 163, 135
 Meegan, C., Lichti, G., Bhat, P. N., et al. 2009, *ApJ*, 702, 791
 Menzel, D. H., & Cillie, G. G. 1937, *ApJ*, 85, 88
 Milligan, R. O., Chamberlin, P. C., Hudson, H. S., et al. 2012, *ApJL*, 748, L14
 Milligan, R. O., Kerr, G. S., Dennis, B. R., et al. 2014, *ApJ*, 793, 70
 Müller, D., St. Cyr, O. C., Zouganelis, I., et al. 2020, *A&A*, 642, A1
 Noyes, R. W., & Kalkofen, W. 1970, *SoPh*, 15, 120
 Pesnell, W. D., Thompson, B. J., & Chamberlin, P. C. 2012, *SoPh*, 275, 3
 Reid, A., Zhigulin, B., Carlsson, M., & Mathioudakis, M. 2020, *ApJL*, 894, L21
 Ricchiazzi, P. J., & Canfield, R. C. 1983, *ApJ*, 272, 739
 Robinson, B. J. 1959, *RPPH*, 22, 241
 Rubio da Costa, F., Kleint, L., Petrosian, V., Liu, W., & Allred, J. C. 2016, *ApJ*, 827, 38
 Shimizu, T., Imada, S., Kawate, T., et al. 2019, *Proc. SPIE*, 11118, 1111807
 Simoes, P. J. A., Kerr, G. S., Fletcher, L., et al. 2017, *A&A*, 605, A125
 Spice Consortium, Anderson, M., Appourchaux, T., et al. 2020, *A&A*, 642, A14
 Vernazza, J. E., Avrett, E. H., & Loeser, R. 1973, *ApJ*, 184, 605
 Vernazza, J. E., Avrett, E. H., & Loeser, R. 1976, *ApJS*, 30, 1
 Vernazza, J. E., Avrett, E. H., & Loeser, R. 1981, *ApJS*, 45, 635
 Watanabe, T. 2014, *Proc. SPIE*, 9143, 914310
 Wilhelm, K., Curdt, W., Marsch, E., et al. 1995, *SoPh*, 162, 189
 Woods, T. N., Eparvier, F. G., Hock, R., et al. 2012, *SoPh*, 275, 115
 Zharkova, V. V., & Kobylinsky, V. A. 1993, *SoPh*, 143, 259